Eurasian Journal of Analytical Chemistry
ISSN: 1306-3057 OPEN ACCESS 2024 19 (1): 575-583

The Influence of Manganese Doping on Zinc Oxide Nanoparticles for Photocatalytic Degradation of Methylene Blue Dye

Aarti Pathak[1]*, Anjali Soni[1], Archana Chaudhary[2], Uday Deshpande[3]

[1]Department of Chemistry, Medi-Caps University, Indore, 453331, Madhya Pradesh, India
[2]Research and Development Cell, Indian Institute of Technology, Indore 453552, Madhya Pradesh, India
[3]Scientist-F, UGC DAE CSR, Khandwa Road, Indore, 452001, Madhya Pradesh, India

***Corresponding Author:** Aarti Pathak
*Department of Chemistry, Medi-Caps University, Indore, 453331, Madhya Pradesh, India
*Email: aarti.pathak@medicaps.ac.in

Abstract
Successful scalable synthesis of Manganese-doped and Pure Zinc oxide nanoparticles (3%, 5%, 7% Mn-ZnO) utilizing a straightforward and cost-efficient combustion method has been done. Once synthesized, the samples were analyzed using X-ray Diffractometer (XRD) to unveil their crystal and lattice parameters, while UV-Vis DRS Spectroscopy will shed light on their optical properties. To further understand their physical characteristics, both the pure and doped nanoparticles will undergo scrutiny via FE-SEM, Energy Dispersive X-ray (EDX) and X-ray Photoelectron Spectroscopy (XPS), techniques. In the next phase, doped nanoparticles were employed as photocatalysts, specifically for photodegradation of Methylene Blue (MB) dye under visible light exposure, with the resulting changes being analyzed using UV-Vis Spectroscopy. Furthermore, parallel experiments were conducted with the presence of an oxidizing agent, Hydrogen Peroxide (H_2O_2), facilitating a comprehensive comparative analysis. This approach promises valuable insights into both the properties of these nanoparticles and their potential applications.

Keywords: Photocatalysis; Zinc Oxide; Nanoparticles; Methylene blue; Dye Degradation; Hydrogen Peroxide.

1. Introduction

The pressing issue of widespread environmental pollution, stemming from extensive human activities, demands urgent attention to safeguard the quality of our environment for future generations. In response to the escalating threat posed by environmental pollutants, significant efforts have been directed towards photocatalytic methods as a promising avenue for their detoxification. Metal oxide semiconductor-mediated photocatalysis has become increasingly appealing as a method to combat environmental pollution, owing to its impressive ability to break down a broad spectrum of inorganic, organic, drugs, and microbial contaminants into harmless byproducts like water, mineral acids, carbon dioxide and under UV light exposure [1, 2, 3]. This effectiveness arises from the surface and size effects, along with the unique properties inherent to these materials [4]. Manipulating the morphology of materials, such as altering the shape and size of doped nanoparticles, allows for fine-tuning of their chemical and physical properties. Heterogeneous photocatalysis has demonstrated remarkable efficiency in oxidizing and mineralizing oxalate anions in water via a conventional water purification technique, especially when synergistically combined with ozonation [5]. Photocatalysis mainly relies on the stimulation of electrons moving from the valence band of a semiconductor towards the conduction spectrum of a photocatalyst with a broad bandgap when exposed to sunlight. This process generates a vacancy in the valence band, referred to as a hole [6, 7]. The catalyst surface, upon exposure to light, triggers photogenerated charge carriers that kickstart redox reactions in the molecules adsorbed on it. This process begins before the exciton is annihilated, effectively breaking down or reducing contaminating molecules into less harmful components. Various semiconductors, including WO_3, CuS, TiO_2, CdS, ZnO, ZnS, SnO, and more, have been recognized for their excellent photocatalytic properties [8, 9, 10]. However, the effectiveness of TiO_2 under visible light is restricted, limiting its broader application in solar energy, especially considering that the UV region accounts for just over one percent of the solar spectrum. Hence, there's a keen interest in extending TiO_2's absorption range into the visible spectrum, where cheaper light sources can be utilized. In parallel, efforts are underway to explore alternatives to TiO_2, with a focus on shifting the band gap energy towards longer wavelengths. Zinc oxide (ZnO) stands out among these alternatives due to its environmentally friendly nature, widespread availability, significant exciton binding energy of about 60 meV, wide direct bandgap of approximately 3.37 eV, and remarkably high melting point of around 1975°C [11, 12, 13]. ZnO is a diatomic in nature substance that has four inherent point defects, namely zinc vacancies, oxygen vacancies, zinc interstitials and oxygen interstitials. These imperfections function as sites for recombination, generating light at particular wavelengths determined by the transitions of charge carriers inside the bandgap of the material [14, 15]. These attributes position it as a key candidate for various applications including photocatalysis, optoelectronic

devices, solar cells, luminescent devices, chemical sensors, and magneto-optical devices [16]. Within the realm of semiconductor nanotechnology, chemical doping emerges as a pivotal area of research for modifying both microstructures and electronic configurations. Studies have observed that introducing a suitable amount of transition metal doping into a semiconductor can induce alterations in several properties including band gap, structure, electrical conductivity and Fermi level [17]. Doping introduces defects that generate additional energy levels positioned between the conduction and valence bands. These impurities function as hotspots that accumulate and retain charges, which leads to a decrease in the rate at which ions recombine and promotes the passage of electrons across interfaces. As a result, the impurities increase the reactivity at the surface. Furthermore, they broaden the palette of wavelengths that could potentially excite them, stretching from ultraviolet (UV) to the spectrum of visible light. This makes it possible for a greater use of the solar spectrum [18, 19]. ZnO, renowned for its efficacy in dye decolorization in textile industries, serves as an exemplary photocatalyst, with its activity further bolstered by the incorporation of transition metals. The primary aim of doping in photocatalysis is to introduce crystal defects that enhance absorption in the visible spectrum. These minor imperfections generate energy levels within the space between both valence and conduction bands. These levels act as stages of intermediary motion for electron movement when they are triggered by light. Transition metal doping, using elements like Fe, La, Mn, and Pd or their ions, enhances visible light absorption by generating energy states within the bandgap, which facilitates electron transitions during photoexcitation [20]. Following an extensive review of the literature, manganese (Mn) emerges as a promising transition metal for the intended target, chiefly owing to its substantial thermal solubility, reported at 10 mol% [21]. Previous studies by various research groups [22, 23] have indicated that Mn doping in the ZnO system can induce both blue shifts (for Mn concentrations below 3 mol%) and red shifts (for Mn concentrations above 3 mol%) in the optical band gap.

This study involved the synthesis of pure and Mn-doped ZnO nanoparticles (NPs) employing a combustion process, selected for its simplicity and cost efficiency. We conducted a comprehensive study to examine the impact of Mn doping on the optical, photocatalytic, and structural characteristics of Zinc Oxide employing various complementary analytical techniques. The efficiency of the manganese-doped ZnO catalyst in degrading down Methylene Blue dye in light exposure was assessed through assessing its degradation rate.

2. Materials & Methods

2.1. Synthesis of Pure and Mn-ZnO

The majority of the reagents were procured from Loba Chemicals in the analytical class and were employed without any additional processing in our studies. Mn-ZnO nanoparticles have been synthesized employing a simple combustion method, with doping concentrations varying at 0%, 3%, 5%, and 7%. Initially, Zinc Acetate and Manganese Sulphate were dissolved in 20 ml distilled water under ambient conditions, followed by stirring. Urea was gradually added to the solution with continuous stirring until a homogeneous mixture was obtained. The solution was then heated at 450 °C for 10 minutes in a muffle furnace. The resulting powder was ground and subsequently annealed at approximately 500 °C for 1 hour in the same furnace. Finally, the synthesized nanoparticles were further ground using a mortar and pestle. Additionally, for comparison purposes, pure ZnO nanoparticles have been synthesized utilizing the similar method and under identical conditions.

2.2. Characterization

We performed structural analysis using X-ray diffraction (XRD) profiles obtained from a D8 Advance powder X-ray diffractometer with a Cu Kα source (λ = 0.15408 nm), operated at 40 kV and 100 mA, at room temperature. The structural alterations in the ZnO lattice caused by different levels of Mn doping were analyzed by comparing the cell parameters across all specimens based on the XRD patterns. Crystallographic data has been collected over a 2θ range of 20° to 80°. Additionally, UV-visible Diffuse Reflectance Spectroscopy (DRS) was employed to determine the optical band gap of the powder samples. Optical absorption spectra, with the wavelength in the range of 200–850 nm, were recorded with $BaSO_4$ used as a reference for background correction. To convert reflectance to absorbance, we applied the Kubelka–Munk function, wherein $F(R) \propto \frac{K}{S} = \frac{(1-R)^2}{2R}$, with K representing the absorption coefficient, S denoting the scattering coefficient, and R indicating the diffuse reflectance. X-ray photoelectron spectroscopy (XPS) was employed to verify the oxidation states along with chemical composition of the samples, utilizing Mg Kα X-ray as a source. Utilizing the C-1s peak at 284.6 eV as a reference, the binding energy in the XPS spectra was calibrated. Surface morphology, particle size, and composition of the photocatalysts were analyzed using a FE-SEM Supra-55 scanning electron microscope (SEM). Additionally, further insights into the morphology and structural properties were obtained through extensive examination with an Energy-dispersive X-ray (EDX) analyzer (Oxford AZtec X-MAX 20).

2.3. Photocatalytic study

The photocatalytic efficacy of produced samples was assessed at room temperatures by observing the decomposition of Methylene Blue dye (MB) in aqueous solutions. To initiate the experiment, 0.033 gm of methylene blue dye was allowed to dissolve in 100 ml of D.I. water, to obtain 1 mM/L stock solution. The nanoparticles were

then dispersed in a solution containing 2 ml of the stock solution, which was diluted in 100 milliliters of deionized water. The suspension was rapidly agitated in the absence of light for a duration of 45 minutes to achieve an adsorption-desorption equilibria involving the methylene blue dye and dissolved O_2 on the surface of the catalysts. Subsequently, the dye solution was subjected to visible radiations using a 50 W halogen lamp as the radiation source, with the visible light filtered through a cutoff wavelength of 420 nm. Following a 30-minute period of exposure to light, 4 ml aliquots were extracted and subjected to centrifugation in order to separate the photocatalyst. The UV-Visible absorption spectrum of supernatant solution was subsequently measured, utilizing the distinctive absorption peak of methylene blue to observe the advancement of the photocatalytic decolorization process. The degradation rate of the dye was determined from the UV-Vis absorbance spectrum for each sample. For comparative analysis, the experiment was repeated with the addition of hydrogen peroxide as an oxidizing agent, and the absorption curve was analyzed using a UV-Visible spectrophotometer. The decolorization efficiency (η) was calculated using the formula: $\eta = C_0 - \frac{c}{C_0}$, where C and C_0 represent the residual and initial concentrations of methylene blue dye, respectively. It's worth noting that no oxygen was introduced into the suspension during the photoreaction process.

3. Result & Discussion

3.1. Characterization

3.1.1 X-ray Diffractometer (XRD):

The XRD spectrum shown in Fig. 01 reveal the structural characteristics of both pure ZnO and Mn-doped $Zn_{1-x}Mn_xO$ (x = 0.03, 0.05, 0.07) nanoparticles. The diffraction peaks unambiguously demonstrate the existence of the hexagonal wurtzite arrangement of ZnO, featuring a space group P63mc, for all samples. This observation is consistent with JCPDS card No. 89-1397, providing confirmation that Mn ions have been successfully integrated into the ZnO lattice. The presence of clear and sharp peaks indicates that the samples exhibit an exceptional crystalline structure. These diffraction peaks correspond to crystalline structures of wurtzite ZnO, as evidenced by the presence of (112), (100), (102), (110), (101), (103) and (002) diffraction peaks. The heightened intensity of the (101) peak suggests preferential growth of nanocrystals along the ZnO crystallization's easy direction [24]. An analysis of the X-ray diffraction (XRD) spectra of Mn-doped ZnO and pure ZnO demonstrates a minor decrease in the strength of the diffraction peaks in the Mn-doped samples. However, no traces of oxides, binary zinc manganese phases, or manganese metal were detected in 5% Mn doped samples, indicating single-phase formation with a hexagonal wurtzite structure. Typically, when an ion of a metal acts as a dopant which further shifts an original lattice ion, XRD peaks exhibit systematic shifts toward either lower or higher angles, depending on the ionic radii. In this scenario, the diffraction peaks undergo a shift towards smaller angles, which can be explained by the inclusion of Mn^{2+} ions into the crystal structure of ZnO. The Mn^{2+} ion has a higher ionic radius of 0.80 Å compared to the Zn^{2+} ion with a radius of 0.74 Å. This difference in size is responsible for the observed peak shift, which indicates changes in the lattice characteristics. It confirms that the substitution of Zn^{2+} by Mn^{2+} in the ZnO lattice was successful. However, the integration of Mn ions into the ZnO crystal structure is not entirely straightforward due to the equilibrium state of the ZnO growth process, which somewhat limits the incorporation of foreign phases [25].

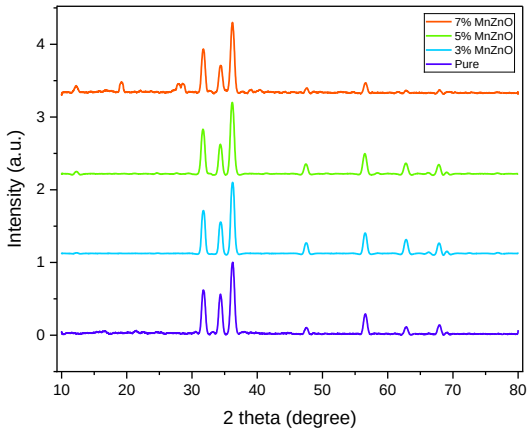

Fig. 01: XRD graph for Pure and Mn-ZnO (3, 5, 7%)

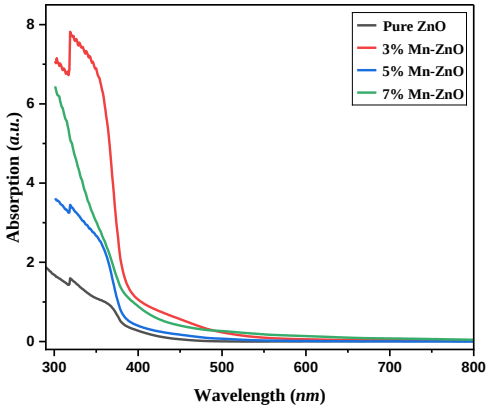

Fig. 02: UV-Vis absorbance graph for Pure and Mn-ZnO (3, 5, 7%)

To acquire more accurate size information about the nanoparticles, we estimated the crystallite size of both Mn-doped and pure ZnO using the Debye–Scherrer formula: $B = \frac{K\lambda}{L\cos\theta}$. In this context, the constant K represents the shape factor (0.94), λ denotes the X-ray wavelength (1.5408 Å for CuKα), θ denotes Bragg's angle, whereas L represents the full width at half maxima (FWHM) of the diffraction peak at θ. The interplanar spacing (d) was calculated using Bragg's Law: nλ = 2d Sinθ, where n is the order of diffraction. We also calculated crystallinity using the formula: $\text{Crystallinity}(\%) = \frac{\text{area of crystalline peaks}}{\text{area of all peaks}}$ Additionally, the grain size was determined using a modified Scherrer equation. The results, including d-spacing, lattice parameters, crystallite size, grain size, and crystallinity, are summarized in Table 01. Comparison with pure ZnO revealed that doping of Mn in ZnO samples led to an increased crystalline size, consistent with previous findings [26]. However, for doped ZnO, our results indicate decrease in the size of the crystallite from 19.27 to 10.40 nm as Mn doping level in ZnO increases, suggesting a dependency on the Mn content within the ZnO crystals of the crystal size of the doped nanoparticles. Additionally, the lattice parameters 'a' and 'c' were calculated from the XRD patterns, and their values closely match the lattice constants of 3.253 nm and 5.213 nm, as referenced in JCPDS No. 81-1397.

Table 01: XRD parameters for Pure and Mn-ZnO (3,5,7%)

Samples	Crystallite size (nm)	Crystallinity (%)	d-spacing (Å)	Lattice Parameter (Å)	Grain Size (nm)
Pure ZnO	14.51	83.41	1.88	a=b= 3.25, c= 5.21	11.18
3% Mn-ZnO	19.27	79.02	1.95	a=b= 3.25, c= 5.21	15.03
5% Mn-ZnO	12.54	80.62	1.97	a=b= 3.26, c= 5.21	9.90
7% Mn-ZnO	10.40	82.78	2.04	a=b= 3.25, c= 5.22	6.02

3.1.2. UV-Vis Diffuse Reflectance (DRS) Spectroscopy:

To determine the optical characteristics of both ZnO and Mn-ZnO nanoparticles (3%, 5%, and 7% doping levels), optical absorption studies were conducted at room temperature. The spectra obtained from UV-Vis DRS for both pure and Mn-doped ZnO nanoparticles are shown in Fig. 2, highlighting the influence of Mn doping on the absorption characteristics across the electromagnetic spectrum. Notably, the Pure ZnO sample exhibits minimal absorbance lying under visible range (λ > 400 nm), whereas Mn-doped ZnO samples display a wide band of absorbance encompassing the whole visible illumination range. This broad absorption band is attributed to d–d transitions from the lower ground state $^6A_1$ to the higher excited states $^4T_2$, $^4A_1$, and ^4E of the Mn^{2+} ions, resulting from the crystal field splitting of the ^4G state of free Mn^{2+} ions within the wide bandgap structure of ZnO [27].

The higher optical absorbance of Mn-ZnO is attributable to an enhanced presence of defect sites in the structure of the crystal as compared to pure ZnO. This observation is consistent with findings in other systems of ZnO doped with metal ions. However, as the concentration of Mn doping in ZnO increases, the absorption edge shifts towards the red end of the spectrum. Previous reports have observed contrasting phenomena, which can be attributed to various factors. These factors include an enhanced exchange interaction between the s as well as p electrons of Zn and the d electrons of Mn, which leads to the formation of new energy levels. Additionally, fusion of the Fermi spectrum into the conduction band, which is made up of ZnO can occur regardless of the carrier concentration. Another factor is a spike in defect densities, such as oxygen vacancies [28]. The modification in the energy band gap within a semiconductor triggered by doping is referred to as the Burstein-Moss shift, which can be significantly amplified by raising the concentration of Mn. The main trigger of the red shift detected in ZnO is the generation of impurity levels introduced by Mn doping. This allows for electronic shifts between those impurity states as well as the valence or conduction band, leading to increased absorption of visible light.

We estimated the band gap energy (Eg) for both pure ZnO as well as Mn-doped ZnO nanoparticles using Tauc's relation, which establishes the correlation between the absorption coefficient and photon energy; $\llbracket \alpha h\nu = A(h\nu - E \rrbracket_g)^{\frac{1}{2}}$, In the present context, the symbol α is used to designate the absorption coefficient, h represents Planck's constant, and ν is defined as the frequency. By projecting the linear section of the $(\alpha h\nu)^2$ against hν curve onto the photon energy (hν) axis, with α equal to 0, it is possible to determine the optical band gap (Eg), as depicted in Figure 03. Using this method, the calculated Eg values for undoped ZnO, 3% Mn-ZnO, 5% Mn-ZnO, and 7% Mn-ZnO were found to be 3.21, 3.29, 3.27, and 3.24 eV, respectively. These findings align well with previously reported results, indicating consistency [29]. The substantial differences in the optical absorption between pure and Mn-doped ZnO suggests that manganese-doped ZnO possesses a greater ability to absorb visible light, therefore presenting itself as a very attractive contender for efficient photocatalysis when activated only by visible light. It is well established that the photocatalytic performance of a photocatalyst is largely determined by its charge separation efficiency, light absorption capability, and the rate of charge transfer to the substrates. Consequently, manganese doping can create conducive conditions for enhancing photocatalytic activity by augmenting ZnO's ability to absorb visible light.

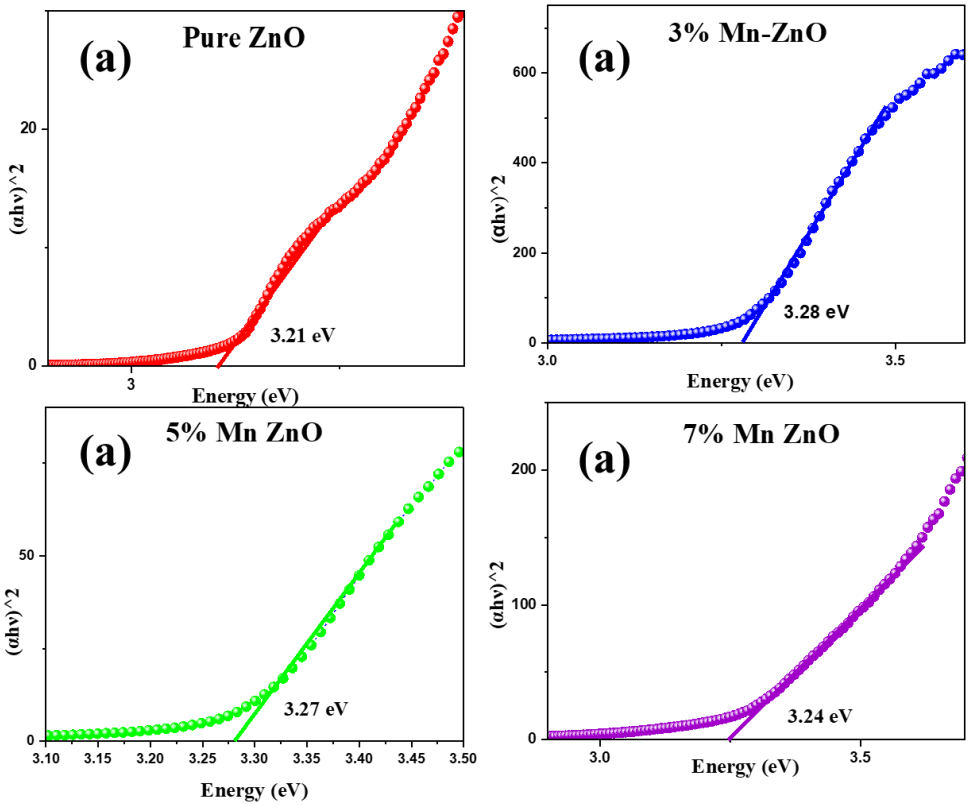

Fig. 03: Tauc Plot for (a) Pure ZnO (b) 3% Mn-ZnO, (c) 5% Mn-ZnO, (d) 7% Mn-ZnO

3.1.3. X-ray Photoelectron Spectroscopy (XPS):

XPS was employed to analyze the electrons emitted from the sample's surface, providing insights into the chemical bonding structure and oxidation states of ions in Mn-ZnO nanoparticles at doping levels of 3%, 5%, and 7%. The XPS spectra representing the valence bands of Zn, O, and Mn are shown in Fig. 04. To correct for any charge-induced shifts in the spectra, the C-1s photoelectron signal at 284.6 eV was used for reference. Three peaks can be seen in the deconvoluted C-1s XPS spectrum: 285.9, 284.6, and 288.5 eV. The C=C bond is associated with the peak at 288.5 eV, whereas the C-O bond is responsible for the peak at 284.6 eV.

The XPS spectra of O-1s exhibit asymmetry, indicating the presence of multiple O_2 species on the surface. Gaussian fittings were applied to deconvolute the curve into three distinct peaks at 529.9 eV, 531.5 eV, and 532.9 eV. The observed peak at 529.9 eV is associated with oxygen in the Zn–Mn–O crystal lattice, while the higher energy peak at 532.9 eV suggests the possible existence of chemisorbed oxygen atom, likely due to surface hydroxyl groups. This analysis provides valuable insights into the surface composition and bonding characteristics of Mn-ZnO nanoparticles, which are crucial for understanding their properties and potential applications.

There were two noticeable peaks that corresponded to Zn $2p_{3/2}$ and Zn $2p_{3/2}$, exhibiting binding energies of 1021 eV and 1044 eV, respectively. Additionally, the primary peaks of Mn $2p_3/_2$ and Mn $2p_{1/2}$ were detected at 642 eV and 651 eV, respectively, indicating the Mn-ZnO system's Zn ions being replaced by Mn ions. Previous studies suggest that the XPS peaks of Mn^{3+} and Mn^{2+} are closely positioned, pointing to the coexistence of both Mn^{2+} and Mn^{3+} in the sample. Furthermore, a satellite peak approximately 5 eV apart from the Mn $2p_{3/2}$ main peak, characteristic of Mn^{2+}, was observed, indicating that Mn^{2+} is more prevalent than Mn^{3+} in the sample. The broadening of the Mn

$2p_{3/2}$ peak further suggests charge transfer between Mn^{2+} and Mn^{3+} within the ZnO matrix. The ZnO lattice has multivalent Mn (Mn^{3+}/Mn^{2+}) incorporated into it, as confirmed by these XPS results.

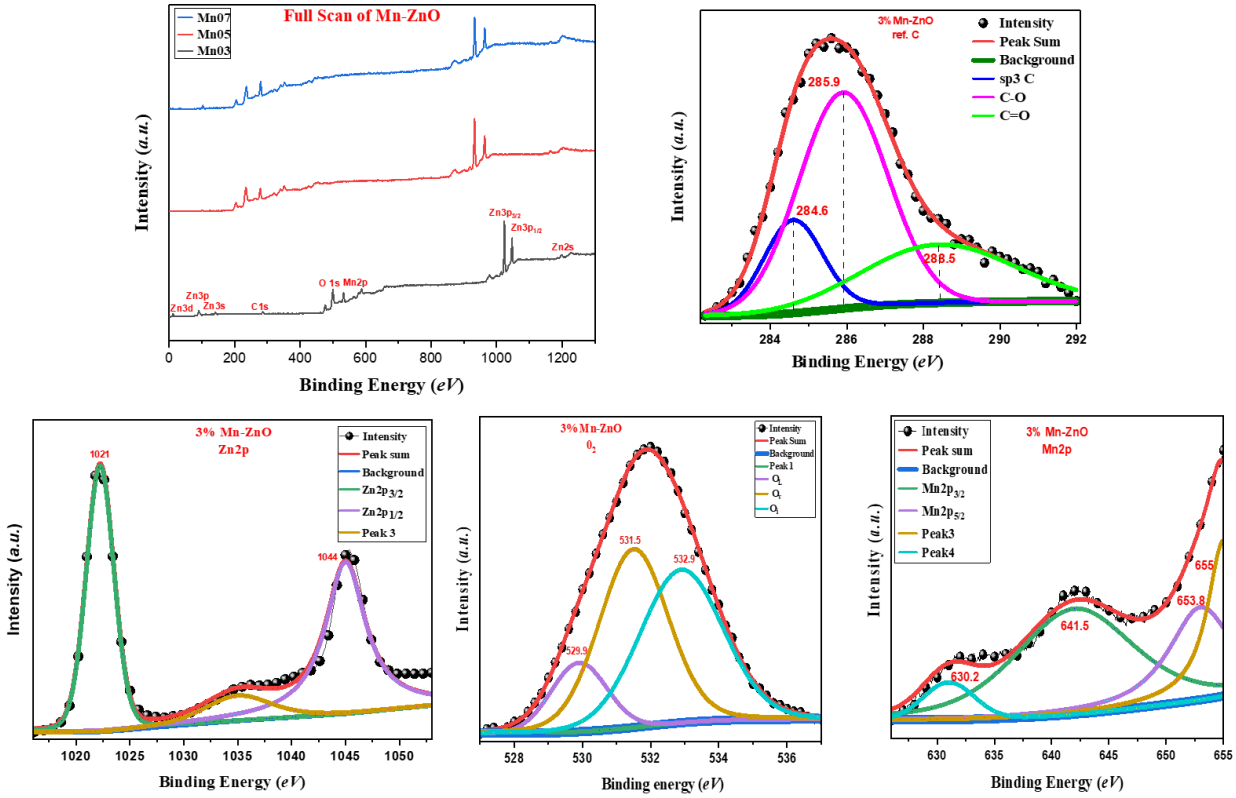

Fig. 04: XPS high resolution spectra of (a) XPS full scan of Mn doped ZnO, (b) C-1s XPS spectrum (c) Zn-2p, (d) O_{2s} and (e) Mn-2p of 3% Mn–ZnO nanoparticles

3.1.4. Scanning Electron Microscopy (FE-SEM):

Scanning electron microscopy (SEM) was used to analyze the surface morphology along with dimensions of the produced pure and Mn-doped ZnO nanoparticles. The SEM micrographs reveal that the Mn-doped ZnO nanocomposites appear as poly-dispersed aggregates with irregular shapes and lack uniformity, consisting of roughly formed particle agglomerates, as shown in Fig. 05. The SEM images showcased seed-like structures of Mn-doped ZnO nanoparticles, consistent with prior findings. Observations from the SEM images indicate that agglomeration increases with higher molar concentration, likely attributable to a kinetic equilibrium process. In this process, the high concentration of Mn dopants may nucleate with oxygen ions independently, leading to the formation of larger particles [32]. Consequently, it becomes challenging for Mn to be incorporated in the ZnO lattice only at higher concentrations. In summary, lower dopant concentrations of Mn-doped ZnO nanoparticles exhibited low agglomeration and a more well-ordered, smaller particle size distribution compared to higher Mn dopant concentrations. The increase in particle size can be attributed to Mn doping.

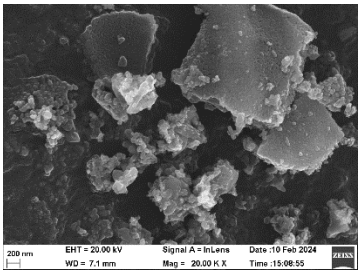

Fig. 05: SEM images for Mn-ZnO

3.1.5. Energy Disperse X-Ray Analysis (EDX) :

Given the limited sensitivity of XRD to small precipitates of secondary phases, additional examination of the samples was conducted using EDX. EDX analysis is crucial for determining dopant concentrations accurately.

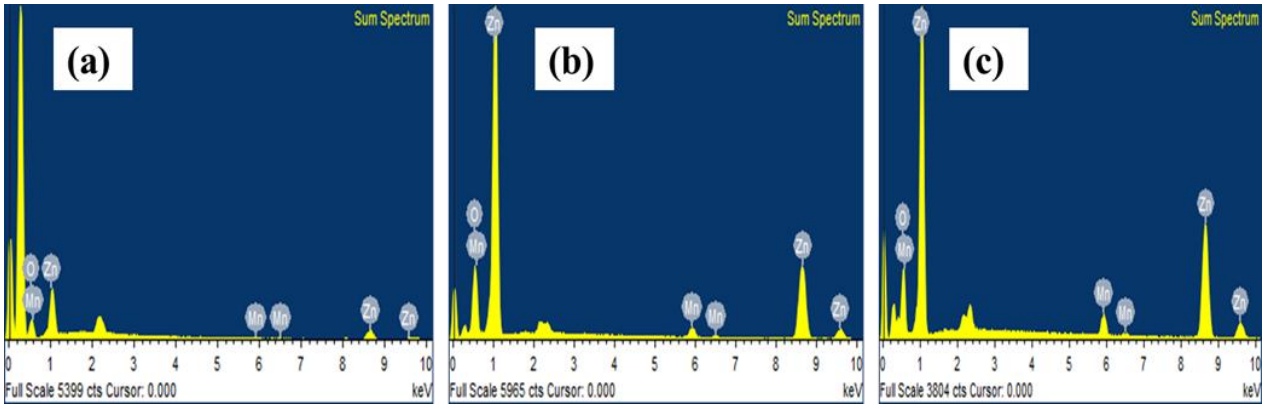

Fig. 06: EDX spectra for (a) 3% Mn-ZnO, (b) 5% Mn-ZnO, (c) 7% Mn-ZnO

Fig. 06 illustrates the EDX spectra of the 3% Mn–ZnO, 5% Mn–ZnO, and 7% Mn–ZnO nanoparticles. The EDX analysis reveals that the samples consist primarily of Mn, O, and Zn elements. The excellent level of purity of the synthesized samples was confirmed by the absence of any unexpected components. Additionally, it was observed that the dopant concentration increased proportionally with the amount of Mn added. The area under the spectral lines provides quantitative Mn/Zn ratio results. The elemental analysis for Mn, O, and Zn for the doped samples is presented in Table 02.

Table 02: EDX parameters for Mn doped ZnO (3,5,7%)

Element	3% Mn-ZnO (%)	5% Mn-ZnO (%)	7% Mn-ZnO (%)
Mn	0.81	3.00	4.71
Zn	46.22	69.04	76.94
O	52.97	27.96	18.35

3.2. Photocatalytic study

To analyze the effect of incorporating Mn^{+} ions into the ZnO lattice on photocatalytic activity, we conducted experiments using methylene blue (MB) dye, a common industrial pollutant, with both pure and Manganese doped ZnO nanoparticles as photocatalysts. The photocatalytic degradation activity was assessed by monitoring the distinctive absorption peak of Methylene blue (MB) dye at 664 nm over time during visible light exposure. The change in MB optical intensity at this absorption peak, as a function of the period of irradiation, is depicted in Fig. 07. The incorporation of Mn atoms resulted in the formation of localized fermi states with lower energy levels inside the bandgap of ZnO. This significantly influenced the photocatalytic properties of Mn-doped ZnO NPs. XPS analysis confirmed the predominant existence of Mn ions within the ZnO matrix, along with various lattice defects including oxygen vacancies and Zn interstitials. These defect sites and dopant ions are expected to introduce localized electronic states within the bandgap, positioned near the band edges [33]. The decolorization of MB began upon visible light illumination of the synthesized semiconductor. Under these conditions, d–d transitions facilitated the transfer of photogenerated electrons from the valence band of Mn-ZnO to the conduction band, leaving charge carriers (holes) in the valence band. These photogenerated holes could then have a reaction with hydroxide ions derived from H_2O to produce hydroxyl radicals ($OH^{\bullet}$). This highly reactive hydroxyl radical generation is crucial for the subsequent decomposition of organic molecules, such as MB, through photo-oxidation. Additionally, photogenerated electrons can be captured by dissolved O_2 molecules, generating superoxide radicals ($O_2^{-\bullet}$), which can subsequently react with H_2O_2 to produce hydroxyl radicals. Hydrogen peroxide serves as a common electron acceptor, enhancing the photocatalytic reaction by increasing the production of hydroxyl radicals in the environment [34]. This increase can occur through several pathways, including direct photolysis of H_2O_2 under UV irradiation, the reaction between H_2O_2 and electrons to produce hydroxyl radicals and hydroxide ions, and the interaction of H_2O_2 with hydroxyl radicals and superoxide radicals that are formed [35].

We investigated the photocatalytic degradation activity of Mn-doped ZnO nanoparticles by varying their concentration in the solution (1 mM and 2 mM). For a comparative analysis, we conducted experiments both with and without the addition of hydrogen peroxide (H_2O_2) to evaluate its effect on the degradation process. The rate of dye photo-decolorization was quantified with the help of the following formula: Decolorization efficiency $\eta(\%) = \frac{C_0 - C}{C_0} \times 100\%$, where C_0 represents the initial concentration of methylene blue dye and C is the concentration after a specific irradiation period. Additionally, we calculated the degradation rate constant using the equation $\ln\left(\frac{C}{C_0}\right) = -kt$, where C_0 denotes the initial MB concentration and C is its concentration at a given time (t = 5 hours).

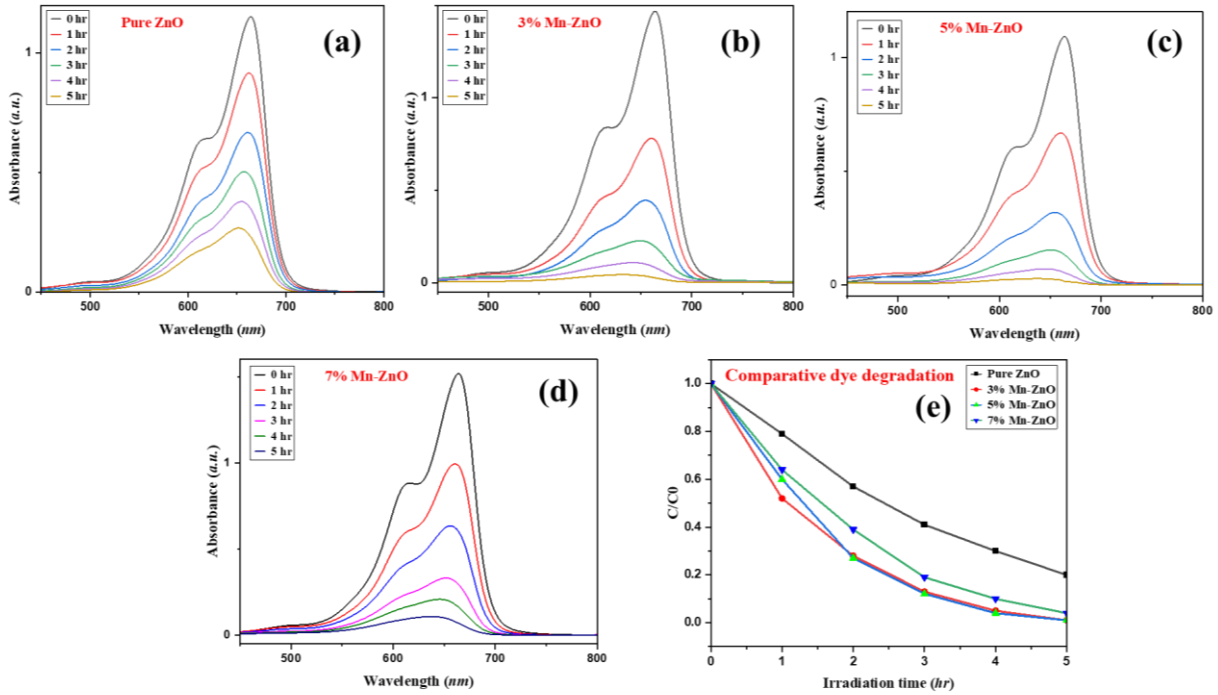

Fig. 07: Absorption spectra of Methylene blue dye for (a) 3% Mn-ZnO, (b) 5% Mn-ZnO, (c) 7% Mn-ZnO (d) pure ZnO, (e) Photocatalytic dye degradation study of Mn doped nanoparticles for Methylene blue dye

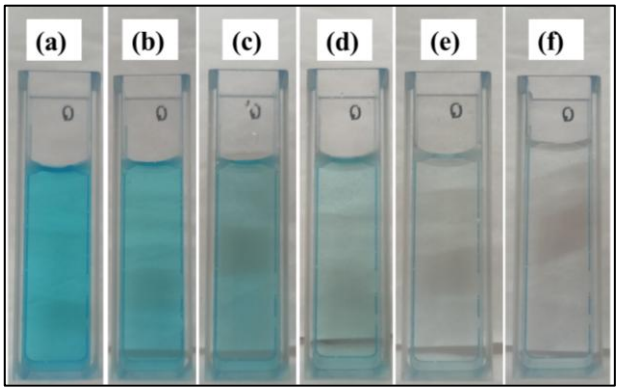

Fig. 08: Photocatalytic Methylene blue dye degradation using Mn doped ZnO NPs in 5 hours

When using 1mM of nanoparticles as a photocatalyst for the degradation process, an unexpected increase in dye absorbance was observed instead of the anticipated decrease. Subsequently, 2mM nanoparticles were introduced into the dye solution and subjected to visible light illumination. Over time, the peak height progressively decreased, indicating the degradation of MB due to the photocatalytic activity of the nanoparticles. These findings suggest that while undoped ZnO alone showed minimal degradation, the incorporation of manganese significantly enhanced the photocatalytic efficiency. The degradation efficiency was quantified as 60.79%, 41.25%, 45.91%, and 44.56% for pure ZnO, 3%, 5%, and 7% Mn-ZnO, respectively, over a 5-hour period. To improve the degradation process, the oxidizing agent hydrogen peroxide (H_2O_2) was introduced under identical conditions. In the presence of H_2O_2, the photocatalytic efficiency of pure ZnO nanoparticles reached 79.96% after 5 hours of visible light exposure. In contrast, the degradation rates for 3%, 5%, and 7% Mn-doped ZnO under the same conditions were calculated as 98.22%, 98.62%, and 95.38%, respectively, significantly exceeding the efficiency of undoped ZnO with H_2O_2. The addition of nearly doubled the degradation efficiency, with 5% Mn-doped ZnO exhibiting the highest values among the nanoparticles under identical irradiation conditions. Furthermore, the degradation process followed first-order kinetics. Notably, the degradation efficiency of methylene blue dye increased with rising Mn doping concentration up to 5%, after which it began to decline. The calculated rate constants in the presence of H_2O_2 for pure ZnO, 3%, 5%, and 7% Mn-doped ZnO were 0.00535 min^{-1}, 0.01344 min^{-1}, 0.01428 min^{-1}, and 0.01025 min^{-1}, respectively. Overall, the 5% Mn-doped ZnO nanoparticles exhibited a significantly enhanced photocatalytic reaction in the presence of H_2O_2, with a rate constant nearly double that of pure ZnO nanoparticles.

4. Conclusion

The combustion method proved to be a convenient and cost-effective approach for synthesizing both pure and Mn-doped ZnO nanoparticles. This method enabled the formation of nanoparticles with a hexagonal wurtzite framework, with an overall crystal size of approximately 14.51 nm. Analysis of XRD data indicated a reduction in crystallite size as the doping concentration increases. The absorption band edge redshifted and the lattice parameter was lowered when Mn+ ions were incorporated to ZnO nanoparticles. XPS analysis of the core level peaks confirmed the presence of Zn^{2+} and Mn^{2+} ions within the hexagonal wurtzite structure of Mn-doped ZnO. With the rise in dopant concentration, the band gap shrank, as demonstrated by UV-Vis DRS spectra. SEM images revealed poly-dispersed aggregates of roughly irregular-shaped particle agglomerates in the synthesized nanoparticles. UV-Vis spectroscopy was utilized to evaluate the photocatalytic activity of both pure and Mn-doped ZnO nanoparticles. The addition of hydrogen peroxide significantly enhanced the photocatalytic degradation efficiency, increasing from 45.91% to 98.62% within 5 hours of visible light exposure. Notably, the 5% Mn-doped sample demonstrated superior performance compared to pure ZnO. In conclusion, ZnO nanoparticles' optical, structural, and microstructural characteristics were significantly modified by the incorporation of Mn, which enhanced their efficiency in the photocatalytic degradation of Methylene Blue dye.

Acknowledgement
Aarti Pathak would like to acknowledge thanks to Medi-Caps University, Indore for granting fellowship under the URF Project Number: URF-MU-2022-06.